Influence of Strain Magnitude on Microstructure, Texture and Mechanical Properties of Alloy 825 during hot-forging

Munir Al-Saadi[1,2,*], Fredrik Sandberg[1], Pär G. Jönsson[2], Christopher Hulme-Smith[2,*]
[1] R&D, AB Sandvik Materials Technology, SE-811 81Sandviken, Sweden.
[2] KTH Royal Institute of Technology, Materials Science and Engineering, SE-100 44 Stockholm, Sweden. * Corresponding authors: muniras@kth.se; chrihs@kth.se

Abstract

Alloy 825 is a nickel-base alloy used in applications with high stresses and corrosive environments. It is commonly hot forged, but there are few data about how this affects the microstructure, which is critical for both mechanical and corrosion performance. Here, Alloy 825 was hot forged in a commercial thermomechanical process to three industrially-relevant strains and the microstucture was examined using scanning electron microscopy and EBSD. Dynamic recrystallization was prevalent, so increasing the forging strain leads to smaller grains. Data were combined to allow each of dislocaiton density, recrystallized grain size and 0.2% proof stress to be calculated as a function of forging strain alone. The grain size or dislocaiton density are related by a powder law finciton with an exponent of ~ -1.5 and the proof stress can be related to either via a Hall-Petch relation. All forging strains were sufficient to meet the criteria of the relevant industrial standard for this material. The maximum yield strength and ultimate tensile strength were obtained after forging to a true strain of 0.9 were $413\ \mathrm{MPa}$ and $622\ \mathrm{MPa}$, respecitvely, with a ductlity of 40%. This may be used to tailor thermomechanical treatments to achieve precise mechanical properties.

Keywords: Alloy 825, Hot forging, Grain structure, Yield strength, Strengthening mechanisms

1. **Introduction**

Alloy 825 is a nickel-based alloy typically supplied in the wrought hot finished annealed bars, or cast into a final shape [1–3]. It is used in pickling tanks and vessels [4], oil and gas industries [5], agitators [6] and heat-exchanger systems [7]. The components in these applications are subjected to a complex combination of elevated temperatures, high stress, and hostile environmental conditions [8]. The high contents of nickel, chromium and molybdenum give good corrosion resistance and high strength. The casting structure is broken down by thermomechanical processing to obtain a uniform chemistry and microstructure. Thereafter, the material is typically subjected to an appropriate annealing process to develop the optimum combination of a good corrosion resistance and mechanical properties [9]. To ensure the mechanical properties and corrosion resistance are suitable for the application, particular attention must be paid to grain size and precipitate populations, as both grain boundaries and precipitates contribute to strengthening, but both grain boundaries the regions around precipitates may be sensitive to chemical attack. Previous work showed that a suitable heat treatment, called a *stabilization treatment* or *soft annealing*, will precipitate the maximum possible volume fraction of Ti(C, N) inside grains. This will provide strengthening while also avoiding the precipitation of $Cr_{23}C_6$-type carbides at grain boundaries, which would deplete regions near grain boundaries of chromium and lead to grain boundary sensitization [9]. In forged products of alloy 825, work hardening, recovery, and recrystallization are possible during hot-forging and stabilization [8,10–15]. It is well known that recrystallization generates fine grains, which is beneficial for both strength and toughness [16–18]. Differences in the grain size within the material are often observed due to inhomogeneous local strains [19]. This can lead to differences in mechanical properties due to variations in both grain size and dislocation density. Therefore, it is important to understand the evolution of strain within the material during the hot forging process. However, there is a lack of research around the behavior of alloy 825 during hot deformation. While some studies do exist, they only focus on dynamic recrystallization at very high reduction ratios (true strain, $\varepsilon_t\colon 0.7 \le \varepsilon_t \le 2.5$) [15]. Industrial processes, in particular hot forging processes, often operate at lower strains, so the results of those studies may not be applicable. The current study addresses this deficiency by examining the effects of lower (industrially relevant) reduction ratios on both microstructure and mechanical properties. The findings should be applicable to all thermomechanical processes at similar tempeatrues and strains.

This article will discuss the application of multiple characterization techniques to conduct a thorough investigation of recrystallization in Alloy 825, which should be applicable to other Ni-Fe-Cr-Mo-Cu alloys. Additionally, the evolution of crystallographic texture has been analyzed. An understanding of the relationships between deformation conditions, thermomechanical history, and crystallographic texture is essential for understanding the resulting properties of forged Ni-based superalloy bar.

The structural strengthening is commonly discussed in terms of Hall-Petch relationship [20]. However, the strength of Alloy 825 and alloys subjected to large strain deformation is rather difficult to express by a simple Hall-Petch equation due to the development of complicated hierarchical microstructure including well developed dislocation substructures with large internal stresses. There are several approaches to evaluate the strength after large strain deformation. Some of them consider the subgrain size as the main strengthening contributor [16,17,19] . Others include the grain boundary and dislocation strengthenings as independent and linearly additive contributors [15,20,21].

The primary objectives of the present work are to understand the microstructral evolution and the dependency of microstructure changes on the deformation level during hot forging of Alloy 825.

2. Materials and methods

2.1 Materials used and thermomechanical treatment

All material in this study came from three billets of Alloy 825, which originated from the same cast ingot (composition in Table 1). The ingots were cast after air melting in an electric arc furnace and refinement using an argon oxygen decarburization process.

Table 1: Nominal composition for the tested material. All values are expressed in wt%. Combustion analysis in accordance with ASTM E1018-11 was used for carbon and nitrogen and X-Ray Fluorescense spectrometry was used for all other elements in accordance with ASTM E572-13.

	C	Si	Mn	Cr	Fe	Mo	Ti	Cu	N	Ni
Alloy 825	0.02	0.20	0.800	22.00	balance	3.000	0.700	1.800	0.018	41.5
Uncertainty	0.01	0.01	0.001	0.03		0.003	0.002	0.005	0.001	0.03

2.1.1 ***Initial microstructure***

The ingot was homogenized at 1200 °C for 6h followed by hot rolling at the same temperature with 80% thickness reduction, after which the material was allowed to air cool. The starting billets (after hot rolling at 1200 °C) had an initial mean recrystallized grain size of 67 ± 3 μm, mesaured using electron backscatter diffraction (EBSD) and the mean linear intercept method. One sample machined from hot rolled billet was separately solution-annealed at 1200 °C for 60 minute in a resistance furnace and then quickly water quenched to simulate the starting microstructure before hot forging.

2.1.2 ***Strain magnitude during hot forging process***

Following established practice, the billets were soaked at 1200 °C for 3 min mm^{-1} and then hot forged. The forging process was performed on a hydraulic press with flat dies and at a strain rate of $\sim 0.5\ \mathrm{s}^{-1}$. The hot-forging of all three billets was performed at temperatures maintained between $950\ ℃$ and $1180\ ℃$ (Fig. 1). Samples were reheated during each forging process and the final forged bars were quenched in water from between $950\ ℃$ and $980\ ℃$. Different samples were subjected to total accumulative strains of 0.45, 0.65 or 0.9 with a pass strain of ~0.1 (i.e. 10% reduction per pass) to study the structural changes during deformation (Table 2). The samples were rotated by 90° from one pass to the next. The true strain was estimated by the formula $\varepsilon = \ln R_{\mathrm{R}}$, where R_{R} is the reduction ratio (ratio of the starting cross-sectional area to the final cross-sectional area). Alloy production and processing took place at Sandvik Materials Technology facilities in Sanvdiken, Sweden. Material was sectioned for microscopy parallel to the forging (axial) direction from the centre of the solid bar.

Table 2: Sample designations used in the current work.

Sample designation	Solution annealed	A	B	C
True strain, ε	0.00	0.45	0.65	0.90

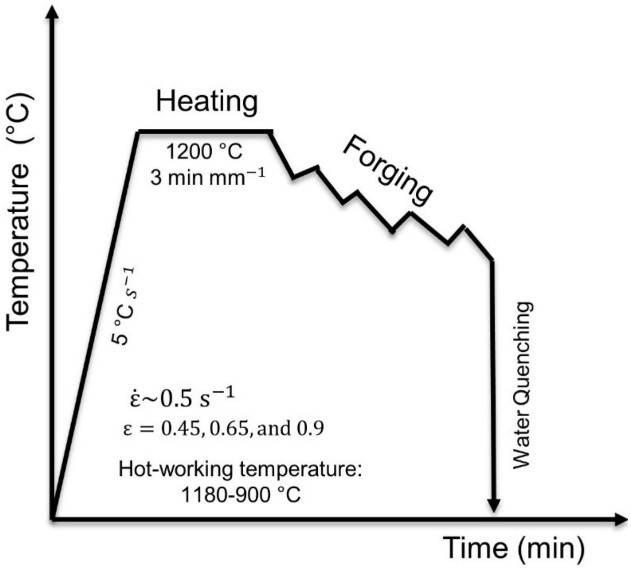
Temperature (°C)
Heating
1200 °C
3 min mm^{-1}
Forging
5 °C s^{-1}
$\dot{\varepsilon}\sim 0.5\ s^{-1}$
$\varepsilon = 0.45, 0.65, \text{and } 0.9$
Hot-working temperature:
1180-900 °C
Water Quenching
Time (min)

Fig. 1—Schematic diagram showing thermo-mechanical processing cycle. “min mm^{-1}” refers to the heat treatment time per millimetre of rod radius.

2.2 Microstructure evolution

2.2.1 Electron backscatter diffraction (EBSD)

Electron backscatter diffraction (EBSD) was conducted using a Zeiss Sigma field emission gun scanning electron microscope (Carl Zeiss Microscopy GmbH, Oberkochen, Germany). The data were acquired and processed using the software TSL OIM Analysis 7 (AMETEK, Inc., Berwyn, PA, USA). The operating voltage was 20 kV. Energy dispersive X-ray spectroscopy (EDS) was also performed to analyse compositions. An orientation imaging microscopy (OIM) map and the misorientation angle of grains were calculated from the EBSD results. The OIM software was used for evaluation of the mean grain size (d) and kernel average misorientation (KAM). Samples for microstructural investigations were mounted in phenolic resin and prepared using standard grinding and polishing procedures. Specifically, the samples were jet polished at temperatures between 8 °C and 18 °C in 3 M sulfuric acid dissolved in ethanol (630 ml ethanol, 123 ml sulfuric acid). The electrolytic polishing voltage, current and time were 30-40 V, 1-2 A, and approximately 30 s, respectively. The areas of observation in this study were in the centre of each sample.

EBSD maps of a solution-annealed sample were obtained for areas 2.313 mm × 1.737 mm with a step size of 3 μm. The EBSD patterns with confidence index below 0.1 were omitted from analysis (such pixels are colored black in images). A total of four scans was used to evaluate the solution-annealed grain size, texture and twin boundaries fraction. The grain size was evaluated by a linear intercept along the forging direction, counting all boundaries with misorientation of $\theta \geq 10°$. To ensure statistically representative results, a minimum of 1500 grains were measured in annealed sample.

A step size of 0.5 μm for higher-resolution local scans was used to characterize the overall deformed microstructure and also subjected to a cleanup procedure, in which only pixels where a confidence index ≥ 0.1 were accepted. The grain size was evaluated by a linear intercept method on orientation imaging maps, counting all high-angle boundaries with misorientation of $\theta \geq 10°$, along the forging direction. The twin boundaries were omitted from the grain size calculations for the recrystallization analysis, whereas the strengthening was analyzed using the grain size including the twin boundaries. To ensure statistically representative results, a minimum of 3000 grains was measured in each deformed sample.

2.2.2 *Identification of dynamically recrystallized grains and dislcoation density*

There are several ways in which EBSD data may be processed. Previous literature has shown that the most reliable technique to identify if a grain has undergone dynamic recrystallization without further deformation is grain orientation spread (GOS) [22], which is the mean difference between the crystal orientation at each pixel within a grain and the mean grain orientation. One mechanism by which a point within a grain may not align with the mean orientation is the distortion caused by the presence of dislocations. Grains that are recrystallized contain few dislocations and so the average distortion will be lower than in a deformed grain that contains many dislocations. In literature, some threshold is applied to classify a grain as either recrystallized or deformed, typically (GOS$\leq 1°$ [22], GOS$\leq 2°$ [23,24], GOS$\leq 2.6°$ [25], GOS$\leq 3.0°$ [26,27], GOS$\leq 5°$ [28]). Grains were defined as each region within which the local misorientation did not exceed 5°, this is the so-called *grain tolerance angle* [21,29]. A minimum size of ten pixels was also set to define a grain. For each sample, at least three EBSD scans with size step of 0.75 μm was acquired, covering an area of 2319 μm × 1737 μm (~4.03 mm^2), 578.5 μm × 434 μm (~0.25 mm^2), and 387 μm × 295.25 μm (~0.114 mm^2).

Dislocation density, ρ, itself is typically measured using a different statistic called the kernel average misorientation (KAM), which is the average difference in orientation between a single point and a set of points that form the boundary of a region used for analysis (the *kernel*). There is a well established equation to relate dislocaiton density to the KAM statistic, known as Frank's rule, which depends on the the kernel average misorientation angle, θ_{KAM}, the Burgers vector of the dislocation density, b, the step size of the EBDS scan, s and a constant that depends on the scanning geometry, κ (Equation 1) [30–32]. There is no such established relationship between GOS and dislocation density, so that technique may not be used here [23,33] .

$$\rho = \kappa\theta_{\mathrm{KAM}}(bs)^{-1} \qquad \text{Equation 1}$$

The KAM step size is used 0.75 µm, which satisfies the requirement that the KAM step size must be smaller than subgrain size (in this case, approximately ~1 µm) in order to provide reliable results for the dislocation density. In this work, the first neighbor was considered for calculating the KAM values.

$\kappa = 2$ represents pure tilt boundaries and $\kappa = 4$ represents pure twist boundaries [32]. Some studies use $\kappa = 2/\sqrt{3}$, as this relates the EBSD step size to the (hexagonal) surface area that is closest to each step location [30,31]. In this study, $\kappa = 2$ is used, as the pixels are in square shape not hexagonal, and as the forging deformation under consideration leads overwhelmingly to the formation of tilt boundaries [34–36]. The dislocation density may, therefore, be calculated from values that are either known (κ, b, s) or may be measured (θ_{KAM}). The kernel average misorientation gives an overestimate of dislocation density because of the presence of low-angle dislocation sub-boundaries that are grain boundaries in practice, but are included in the dislocation density calculation [30,31].

2.2.3 Recrystallized grain size and twin boundaries

Grain boundaries were identified from EBSD data as high-angle boundaries with misorientations, $\theta \geq 10°$ when observed on the plane at $90°$ to the forging axis. The mean grain size was measured by applying the linear intercept method measured on an EBSD map. Boundaries identified as low-angle ($\theta < 10°$) were attributed to sub-grain boundaries formed from regions of high dislocation density and not considered grain boundaries. For each sample, at least three EBSD scans with size step of 0.75 µm was acquired, with each map covering an area 2319 µm x 1737 µm, and used to evaluate the deformation texture and the number of twin boundaries. To ensure statistically representative results, a minimum of 3500 grains was measured in each deformed sample. The microstructure and data reported in this study is a representative microstructure or average of the values obtained from these scans/maps.

The TSL OIM Analyzer software was also used to identify twin boundaries in order to be ignored (excluded) from grain size calculations. Twin boundaries were defined when the misorientation angle, $\theta_m = 60°$ and the local orientation lies within 5° of a $\langle 111 \rangle$ axis. For the grain boundary analysis, boundaries with a misorientation between $2°$ and $10°$ were considered to be low-angle grain boundaries. High-angle grain boundaries were further classified into $\Sigma 3$ (twin boundaries) and other high angle boundaries. Boundaries with a misorientation angle, θ_m: $10° < \theta_\mathrm{m} < 60°$ are characterized by near random distribution. The maximum deviation from the ideal orientation for $\Sigma 3$ boundaries was $8.66°$ according to the Brandon criterion [37]. A fraction of $\Sigma 3$ boundaries was calculated as a ratio of the length of $\Sigma 3$ boundary segments to the total length of all high-angle grain boundary segments. A ratio of the length of $\Sigma 3$ boundaries to the scan area was used to obtain a density of this boundary type.

2.2.4 Crystalographic texture

The texture and misorientation analysis was performed on regions containing fully recrystallized grains and separately on the overall microstructure, including grains that were not recrystallized. The classification of recrystallized and non-recrystallized regions in current analysis was based on the grain orientation spread (GOS) of individual grains.

2.2.5 Estimation of stacking fault energy, γ_{SFE}

In the current material, the stacking fault energy, γ_SFE is calculated as a function of composition (Equation 2, where the symbol for each element represents the content of that element in wt%) [38,39].

$$\gamma_\mathrm{SFE} = 1.59\mathrm{Ni} - 1.34\mathrm{Mn} + 0.06\mathrm{Mn}^2 - 1.75\mathrm{Cr} + 0.01\mathrm{Cr}^2 + 15.21\mathrm{Mo} - 5.59\mathrm{Si} - 60.69(\mathrm{C} + 1.2\mathrm{N})^{0.5} + 26.27(\mathrm{C} + 1.2\mathrm{N})(\mathrm{Cr} + \mathrm{Mn} + \mathrm{Mo}) + 0.61[\mathrm{Ni}(\mathrm{Cr} + \mathrm{Mn})] \quad \text{Equation 2}$$

2.3 Tensile specimens and testing

Three tensile specimens were used for each hot forging condition. Longitudinal samples for microstructural examination and tensile testing were extracted from a location at center and in distance approximately 3 times the outer diameter of a bar (~250 mm) from a hot-forged end surface.

The tensile specimens were machined from the bars processed at different conditions and parallel to the forging direction. Round bar specimens with 10 mm diameter and 50 mm gauge length were used. The room temperature tensile tests were carried out at a strain rate of 0.001 s^{-1} on screw-driven Instron 4488 electromechanical tensile test machine. The yield strength, σ_{Y}, ultimate tensile strength, σ_{UTS}, and total elongation at failure, e_{f}, were determined from the output of the testing machine form software provided by Inersjö Systems AB. To compare the results of orientation measurements before and after tensile testing, all parameters used for the EBSD measurements were kept the same.

2.4 Hardness testing

The average hardness was determined after testing a minimum of ten readings from each processing condition. Hardness testing was performed with Vickers method with a 500 g load in accordance with ASTM E384. The hardness measurements were carried out using an automated universal hardness testing machine (QATM, Qness 30 A+, ATM Qness GmbH, Mammelzen, Germany).

2.5 Transmission electron microscopy

Transmission electron microscopy was used to characterize the microstructure of the as-wrought material (i.e. before initial heating). Imaging was performed using a Tecnai F20 scanning transmission electron microscope (STEM) from Thermo-Fisher Scientific using a 200 kV accelerating voltage with a high angle annular dark field detector. Selected area electron diffraction in the same orientation was used for careful dark-field imaging to identify precipitates for compositional analysis by energy-dispersive X-ray spectroscopy (STEM-EDS).

3. **Results**

3.1. Initial microstructure before hot forging

Fig. 2 shows the initial solution-annealed microstructure with the mean initial grain size (d_0) 122 ± 11 µm, if twins are ignored for the purpose of measuring grain size. The material contians a small number of large grains, between 180 µm and 500 µm in size, together with a large number of much smaller grains, and exhibits annealing twins (Fig. 2a). Twin boundaries (Σ3, red) are common in the microstructure and represent 52.7 $\pm 2.2\%$ of all boundaries. Lower-coincidence boundaries (Σ9, yellow) make up approximately 1.1 $\pm 0.3\%$ of boundaries and the remainder of boundaries are high angle grain boundaries (black). The grains appear to be equiaxed with a strong fibre texture of $\langle 112 \rangle$ along the forging direction (FD). Cubic precipitates could be observed in the body of several grains (Fig. 3). Energy dispersive X-ray spectroscopy analysis suggested a composition of 79.3 ± 0.3 wt% Ti, 20.0 ± 0.3 wt% N, and 0.7 ± 0.2 wt% Cr; carbon was not detected.

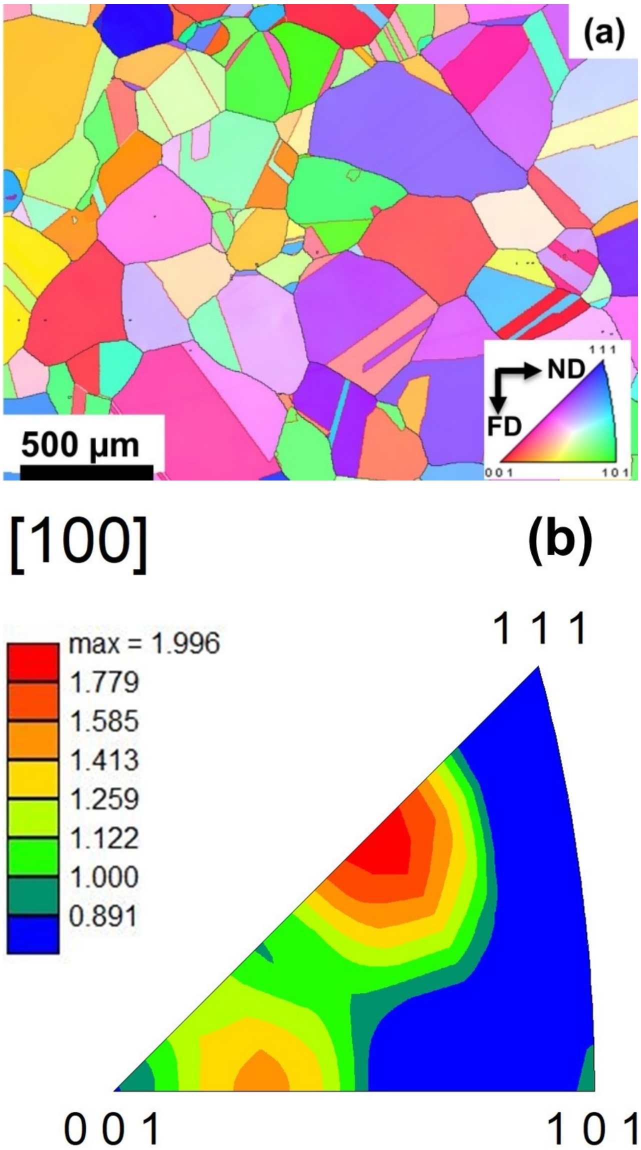

Fig. 2—(a) Inverse pole figure map parallel to forging direction (FD). Twin-type boundaries are highlighted in red, lower-coincidence low-angle boundaries are presented as yellow and high angle grain boundaries are black. (b) Pole figure showing the distribution of crystallographic poles oriented parallel to the forging direction (FD) for Alloy 825 solution-annealed at 1200 °C for 3 min mm^{-1}, as used in this study prior to hot-forging.

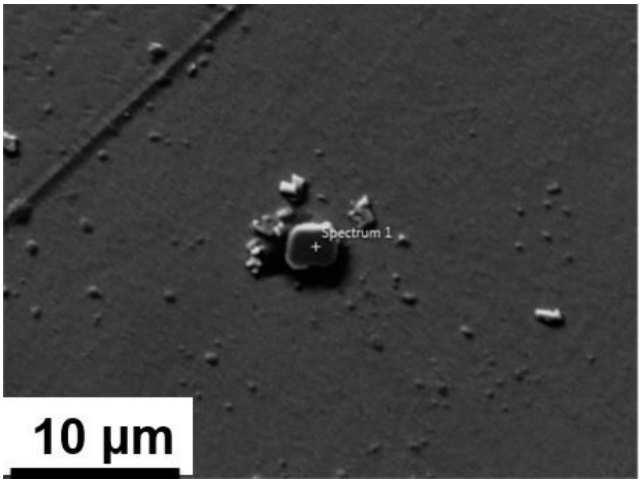

Fig. 3—Secondary electron SEM image of the morphology of a titanium nitride precipitate in the grain interior.

3.2. Evolution of microstructure under strain

Inverse pole figures taken perpendicular to the forging direction (FD) from the highly deformed zones of the as hot-forged samples show the microstructures after the three different levels of deformation (Fig. 4). The iamges show a range of microstructural features, including recrystallized grains, grain boundaries, twins, subgrain boundaries. It is apparent that the as-forged microstructure consists of equiaxed recrystallized grains in a narrow range of sizes a high proportion of twin boundaries and high angle grain boundaries, but is almost free of subgrain boundaries (Table 3, Fig. 4a). Samples B and C (true strain levels of 0.65 and 0.9, respectively) also contain intergranular equiaxed grains. After strain to a level of 0.65, the original equiaxed grains are almost identical to those in the starting microstructure (Fig. 4b cf. Fig. 4a), with the exception that there are more subgrain boundaries (subgrain size ~10 μm) (arrows in Fig. 4b). Following strain to a total level of 0.9, subgrain boundaries (subgrain size ~2.5 μm), large non-recrystallized grains (arrows in Fig. 4c) and very fine recrystallized grains can be observed at a strain level of 0.9. Overall, increasing the total deformation strain leads to an decrease in prevalence of high-angle grain boundaries (Table 3). Increasing the strain level from 0.45 to 0.90 has resulted in approximately half as many Σ3 twin boundaries. The number of high-angle boundaries also decreases sharply, which implies that low-angle boundaries become more prevalent.

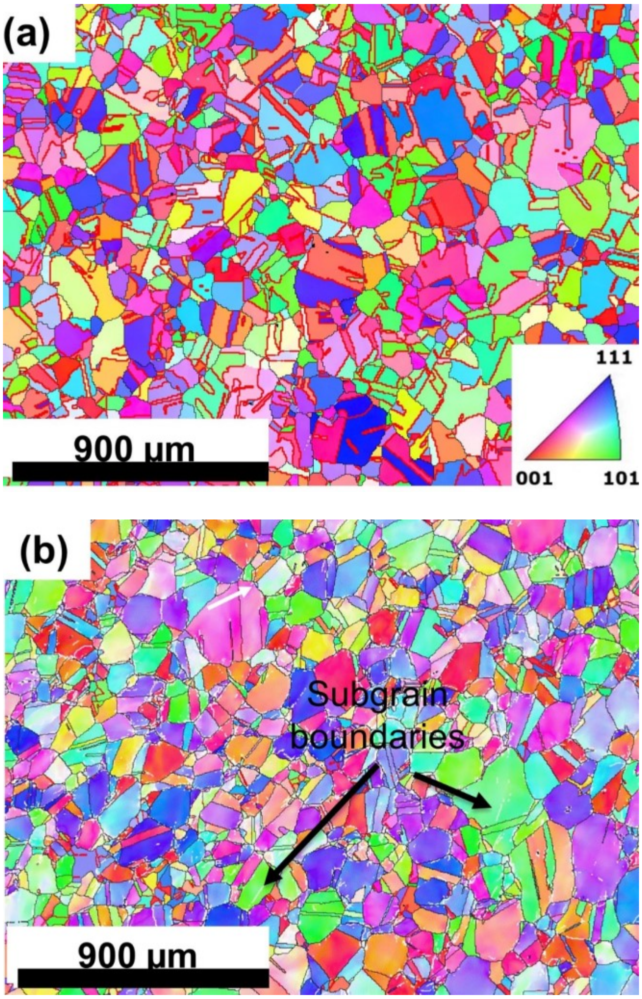

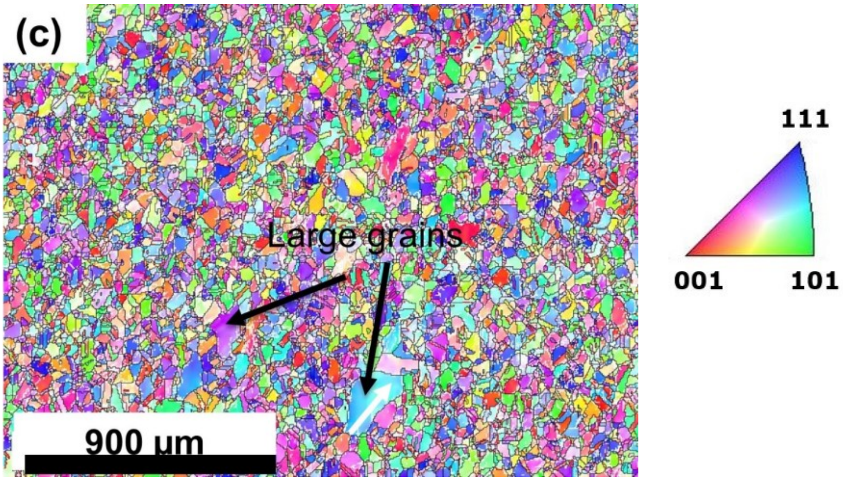

Fig. 4—Inverse pole figure maps measured using EBSD parallel to the forging axis of the as-forged microstructures deformed to deformation level of (a) $\varepsilon = 0.45$, (b) $\varepsilon = 0.65$, and (c) $\varepsilon = 0.9$. Each image is overlaid with high angle grain boundaries (black), low angle grain boundaries (white), and twins (red lines). The white arrows indictate directions for measurment of local misorientations presented in Fig. 6.

Table 3: The mean of recrystallized grain size (diameter) of sample A, B, and C.

	Sample A	Sample B	Sample C
Percentage of grain boundaries that are high angle grain boundaries (includes $\Sigma 3$ twin boundaries)	99.0 ± 0.1	66 ± 16	61 ± 9
Percentage of grain boundaries that are $\Sigma 3$ twin boundaries	57 ± 5	27 ± 4	26 ± 1
The grain size ratio (d/d_0)	0.33 ± 0.06	0.29 ± 0.06	0.18 ± 0.01

3.2.1 Grain refinement

The mean size of the grains of the equiaxed grains, d, are 40 ± 7 μm, 35 ± 7 μm, 22 ± 3 μm for samples deformed to a total strain of 0.45, 0.65, and 0.9, respectively. The large grains in samples are larger than 125 μm (Fig. 4c). All samples contained a plurality of grains that are ~ 25 μm and the grain size distribution of each sample shows a progressive decrease in frequency as grain size increases (Fig. 5).

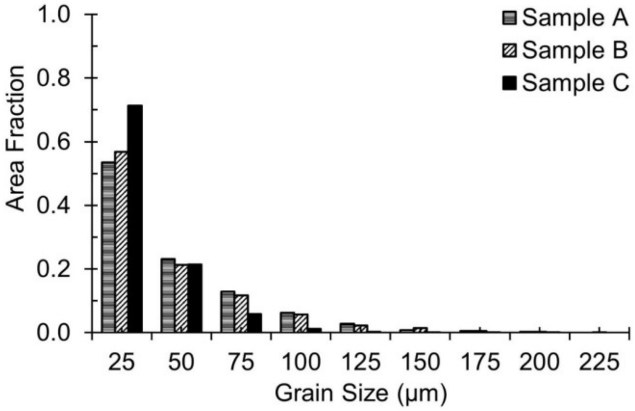

Fig. 5—Distributions of grain size in the as-forged Alloy 825 bar after various strain levels.

3.2.2 Misorientation within grains

Analysis of the crystallographic misorientation in the deformed material (using the data from Fig. 4), shows that the large grains in sample B has an abrupt change in orientation of 60°, which is indicative of a twin. The twin in question is straight-sided, implying that it is an annealing twin that has survived the thermomechanical treatment. The same sample also exhibits a gradual increase in misorientation, relative to the starting point, which implies the present of dislocations. However, in sample C, the misorientation increases gradually to a similar level, but does not show any abrupt change and accumulates across the grain (Fig. 6b). This implies a similar accumulation of dislocations but not twins. Examination of the misorientation between adjacent measurements point (essentially the magnitude of the differential of the total misorientation to the starting point), shows a near-constant value.

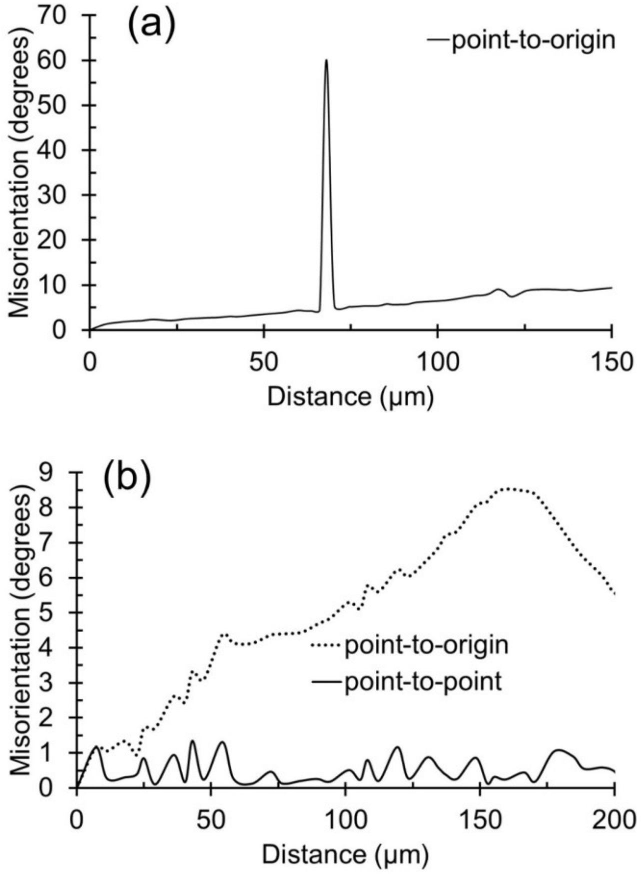

Fig. 6—Misorientations within the grains evolved during hot-forging for (a) sample B (b) sample C along the white arrows indicated in Fig. 4 b and c, respectively.

3.2.3 Dislocation density and recrystallization hot-deformed samples

Total area and grain orientation spread (GOS) was used to distinguish grains that had undergone recrystallization and no subsequent deformation from those that had either recrystallized and had undergone subsequent deformation, or not recrystallized at all (Fig. 7). For $\mathrm{GOS} \leq 1°$, the solution-annealed sample and sample A (deformed to a total strain of 0.45) show only one prominent peak that begins at $0°$ and persists up to $0.6°$. However, the more severely deformed specimens B and C (deformed to a total strain of 0.65 and 0.9, respectively) exhibit grain area distribution with $\mathrm{GOS} > 1°$.

This implies that no grains in samples B and C show high densities of dislocaitons. It also shows that while some grains have high dislocation densities in samples subjected to higher levels of strain, others do not. It is unlikely that strain would be concentrated in a few grains due to deformation, but the findings are explained by recrystallization. Based on the findings for the undeformed sample, it is assumed that all GOS values below 1° imply that grains are non-deformed or recrystallized. This value is consistent with published literature [22,40,41]. However, a threshold value of up to 3° has been reported [27,40] Grains with a GOS $> 1°$ were considered to be deformed – either they did not undergo recrystallization or they recrystallized and then underwent subsequent deformation.

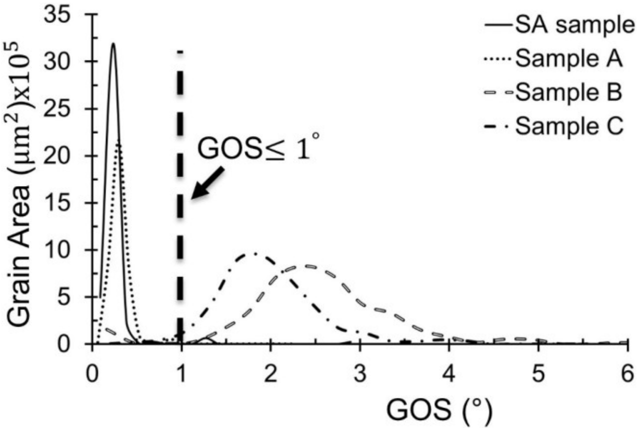

Fig. 7—Grain orientation spread (GOS) plotted agianst the total area of the analysed microstructure that had that GOS at various strain levels from 0.0 (“SA sample”) to 0.9 (Sample C).

3.2.4 Influence of strain magnitude on grain boundary type

However, an increase in deformation level in forged samples B and C led to decreases $\Sigma 3$ twin boundaries (Table 3), containing a large number of sub-grains (low angle grain boundaries, LAGBs). Results indicate that annealing twinning can occur in the present alloy during hot forging even at such a high deformation level (Fig. 4, red lines) [42]. Twinned grains in these samples also contain large internal distortions after hot forging.

Sample A shows a large prevalence (57%) of grain boundaries with a misorientation of 60° (Fig. 8a), corresponding to annealing twins, as well as other high angle boundaries. Very few boundaries are low-angle grain boundaries. An increase in the strain level leads to an increase in the fraction of low angle boundaries: the grain boundary misorientation distribution for both samples exhibits two sharp peaks corresponding to low-angle boundaries and twins (Fig. 8b and 8c). The misorientation distribution outside these two peaks resembles a random distribution [43], albeit not as high, since much of the distribution lies in the two peaks.

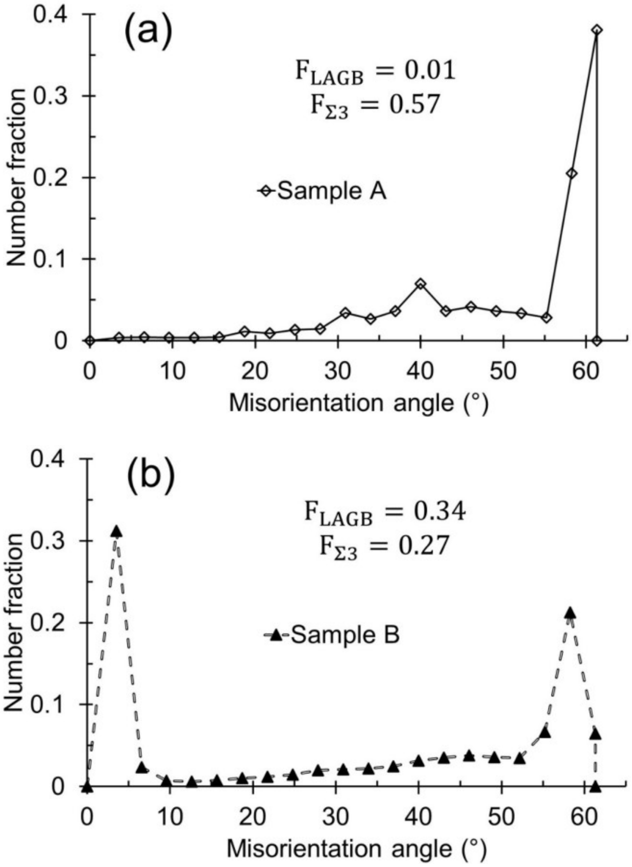

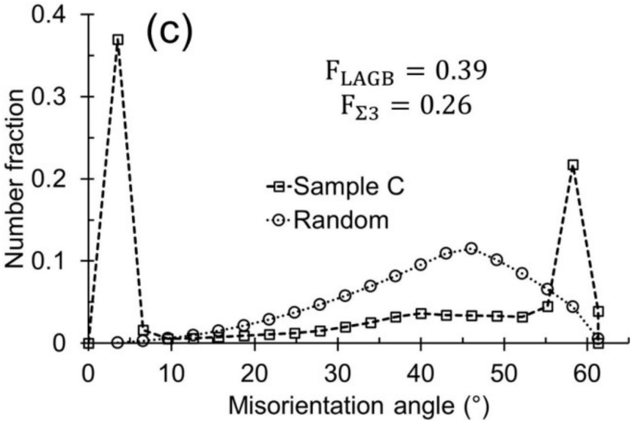

Fig. 8—Misorientation distributions for grain boundaries evolved in alloy 825 subjected to hot forging in (a) sample A, (b), sample B and (c) sample C. The distribution for a random misorientation has been calculated [43] for comparison to sample C.

3.2.5 Deformation Textures

Once grains were identified as recrystallized or deformed, they were analyzed for texture evolution for different strain levels during hot forging. The evolution of different texture components was carried out separately for both deformed and recrystallized regions, and overall microstructure. Whereas the undeformed sample showed no strong texture (Fig. 2), crystal orientation maps of hot-forged samples perpendicular to the forging direction (FD) show that at low strain, where recrystallization was not as prevalent, showed an extremely strong intensity for both $\langle 111\rangle$ and $\langle 102\rangle$ orientations, with both being about five times as strong as would be the case for a random texture (Fig. 9). The highest intensity parallel to $\langle 111\rangle$ is consistent with stable deformation in a face-centered cubic metals. Within recrystallized grains, there is a seemingly random texture, in which the maximum intensity of any one orientation is not more than double that of a purely random texture. This is consistent with a lack of deformation in those grains.

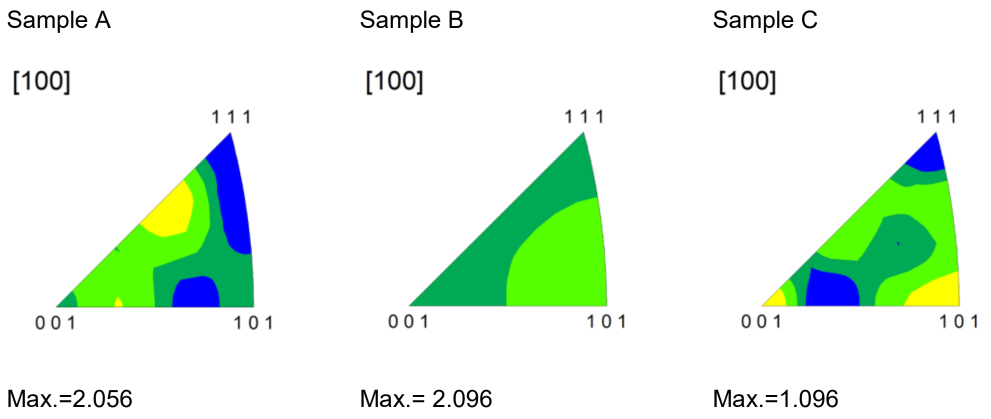

Texture of the overall microstructure

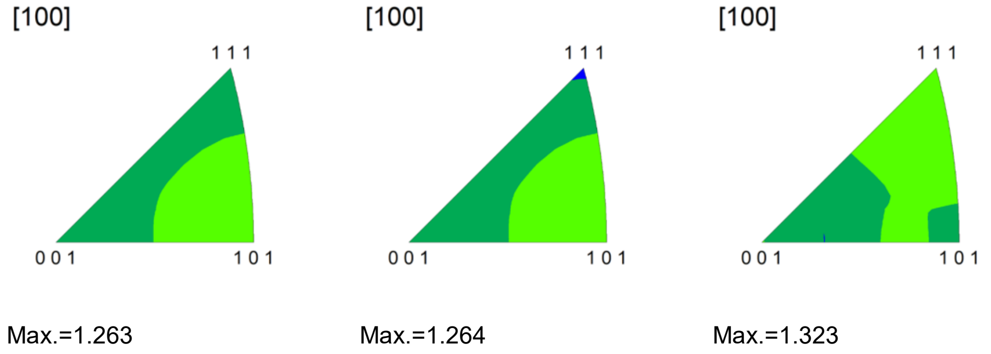

Texture of recrystallized grains

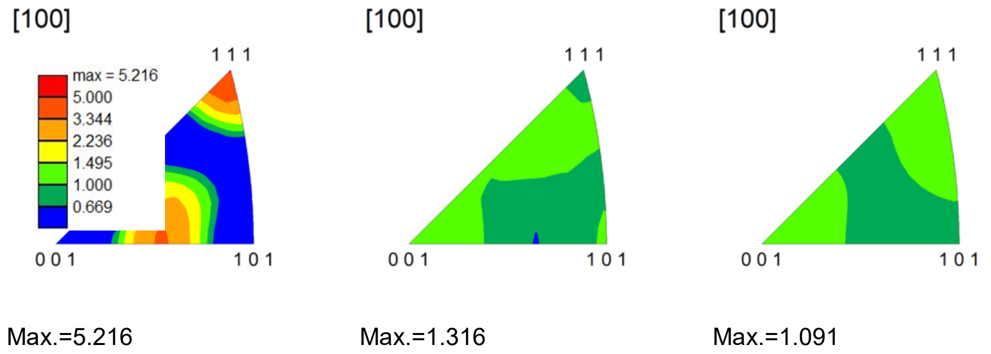

Texture of non-recrystallized grains

Fig. 9—Pole figures of the hot-deformed samples A, B and C. The color map used to show the pole intensities is shown in the inverse pole figures and is used for all subfigures. The maximum intensity

in the pole figure is given below each figure. The direction indicated is perpendicular to the plane of the pole figure.

3.3. Room-Temperature tensile Properties

An increase in strain level leads to significant strengthening of Alloy 825 (Fig. 10). The effect of strain level on the 0.2% proof strength, $\sigma_{0.2}$, is much more pronounced than that on the ultimate tensile strength, σ_{UTS}. The former increases by approximately one third from 305 MPa to 413 MPa, while the latter increases by only 5% from 593 MPa to 622 MPa. This increase correlates with a twofold decrease in the grain size ratio (d/d_0) during section forging (Table 3). For comparison, the available data are also presented [44–48]. The deformation level at which the ultimate tensile strength is recorded decreases with an increase in the deformation level (Fig. 10a), as does the ductility of the samples (Fig. 10a, Table 4). However, all samples show uniform elongation to large plastic strains, up to 0.3, (Fig. 10b) and meet the requirements for the *Standard specification for Ni-Fe-Cr-Mo-Cu alloy UNS N08825 forgings, annealed* [2].

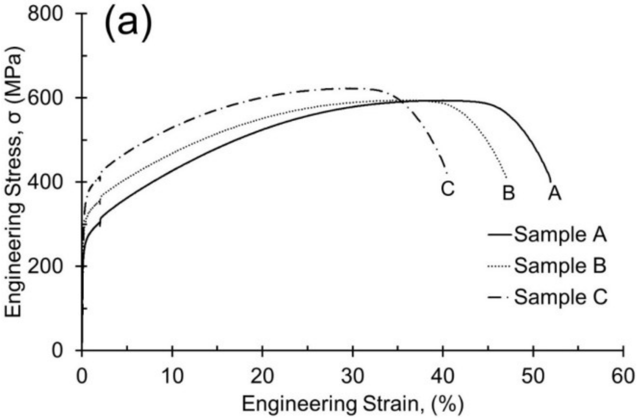

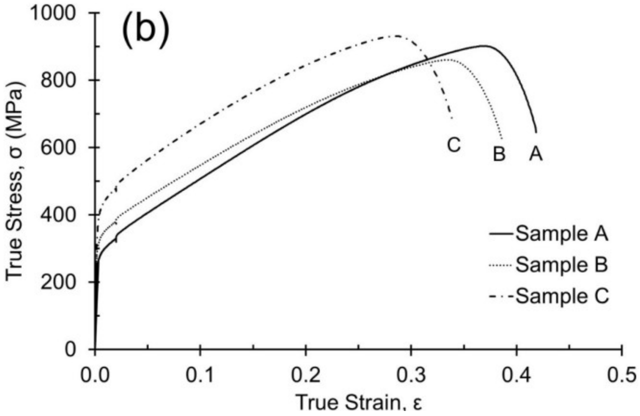

Fig. 10—(a) Engineering tensile stress–strain (b) and true stress–strain curves for Alloy 825 processed by hot forging at indicated samples. All the samples statisfy the minimum yield strength of 241 MPa [2].

Table 4: Room temperature mechanical properties of as-hot forged samples.

Sample	0.2% Proof stress / MPa	Ultimate Tensile Strength / MPa	Failure strain, ε_f (%)
A	305 ± 8	593 ± 3	52 ± 3
B	355 ± 5	594 ± 2	47 ± 2
C	413 ± 5	622 ± 2	40 ± 2

4. **Discussion**

4.1. ***Microstructural evolution***

The reduction of grain size with increasing forging strain is consistent with similar thermomechanical treatments in the temperature range at which recrystallization is possible [49]. The microstructure that develops after hot forging (Fig. 4) is typical of the development of discontinuous dynamic recrystallized grains [50,51]. All three forged samples contain both fine and coarse grains. One potential explanation for this in general materials science is abnormal grain growth [52–55]. However, in the current study, the material is deformed and allowed to recrystallize without large amounts of any second phase to pin grain boundaries (Fig. 2) or any other external factor that would favor one grain orientation over others, such as a magnetic field. Therefore, abnormal grain growth can be rejected as the cause of the grain size distribution in the current study. It is more likely that incomplete dynamic recrystallization is responsible for the grain size distribution: grains that did not undergo recrystallization simply grew during the thermomechanical treatment and correspond to the coarse grains observed after treatment. Those that did recrystallize are significantly finer. This is supported by the reduction in grain size with increasing forging strain, similar to the findings of Niikura et al., who considered the case of a severely-rolled 42 wt% nickel-based alloy ($0.7 < \varepsilon < 2.5$) during hot-working between 1150 ℃ and 950 ℃ [15]. Similar relations also apply to steels containing manganese and copper-nickel alloys, both of which also have a matrix with a face-centered cubic crystal structure [56]. This implies that the same approach may be extended to the current alloy. The presence of the observed subgrain boundaries inside grains is evidence of the progress of continuous dynamic recrystallization (CDRX), strain-induced grain boundaries, (dynamic recrystallization by progressive lattice rotation), where recrystallized grains also can nucleate in the body of prior grains [57]. Also, a varity of small and large dynamic recrystallized grains as well as large deformed grains overall forged microstructure is also evidence of the discontinuous dynamic recrystallization (DDRX) [51]. Since most of the decrease in twin prevalence occurred from sample A to sample B it seems that most twins are destroyed between a strain of 0.45 and 0.65 early in the deformation process. The change in the orientation along the white arrow indicated in Fig. 6b is represented in Fig. 4c. The lattice curvature over the grain (point-to-origin) achieves 9 degree, although the misorientation between any neighboring points (point-to-point) does not exceed 1.5 deg. The selected grain in Fig. 4c contains annealing twins that suggests its discontinuous recrystallization origin, i.e., nucleation followed by growth in course of dynamic or post-dynamic recrystallization. The large internal distortions as shown in Fig. 4c suggest dynamic or post-dynamic recrystallization [19,58–60]. The large internal distortions as shown in Fig. 4c testify to rather high dislocation densities evolved in the alloy samples subjected to hot forging irrespective of discontinuous recrystallization taking place during and/or after deformation.

4.2. ***Texture evolution***

The lack of $\langle 111\rangle$ orientations in the recrystallization texture at all strain levels may have been caused by dynamically recrystallized grains that, after nucleating, rotated toward the hot-forged texture under subsequent deformation [61]. Some studies have proposed that the randomness in recrystallized textures of low stacking fault energy materials is caused by annealing twins, which may hinder recrystallized texture development [62]. This is consistent with both the orientation maps (Fig. 9) and the pole figures of the samples (Fig. 4). It can be seen that the measured textures are weak, with a maximum intensity of not more than double that of a random texture (Fig. 9). Coryell et al. [61] have reported somewhat similar results from nickel-superalloy 945 after the uniaxial compression testing and have shown by EBSD that after deformation to a strain of 1.0 at temperatures 950°C-1150 °C and strain rates of 0.001-1.0 s^{-1}, the microstructure consisted of recrystallized grains that were randomly oriented and contain twins as well as the $\langle 111\rangle$ components were not present in most deformation conditions. Furthermore, the peak in the misorientation angle distribution plots (Fig. 8, sample A) correspond to a 60° misorientation, as has clearly been shown in the misorientation axis distribution in Fig. 9 (Sample A), that is a characteristic of coherent twin boundaries [63]. The decrease in the fraction of $\Sigma 3$ twin boundaries with increased strain level is due to the formation of subgrain boundaries with a misorientation angle between 2° and 10° (low angle grain boundaries) during straining. This is in stark contrast to materials thermomechanically processed by severe plastic deformation $(\varepsilon \sim 3)$ [64].

In the current material, the stacking fault energy (SFE) was calculated to be $88 \pm 5\ \mathrm{mJ\ m^{-2}}$ [38,39,65], which is close to other values in similar face-centred cubic crystal materials, such as copper ($78\text{-}80\ \mathrm{mJ\ m^{-2}}$ [52]). As a result, the primary deformation mechanism is slip, but twinning may also occur at low temperatures and high strain rates [52]. Twinning is also the preferred deformation mode during rolling in regions oriented at $\{112\}\langle 111\rangle$ and $\{100\}\langle 001\rangle$ [52]. For face-centred cubic metals, a $\langle 110\rangle$ texture is most frequently reported but in some low stacking fault energy materials $\langle 111\rangle$ components also form [52].

4.3. ***Effect of strain level on the recrystallized grain fraction, F_G***

The fraction of recrystallized grains (F_G) can be described using a simplified version of the Johnson–Mehl–Avrami–Kolmogorov equation (Equation 3) [66,67]:

$$F_\mathrm{G} = 1 - \exp(-K\varepsilon^n) \qquad \text{Equation 3}$$

where F_G is the fraction of grains, K and n are material constants and depend on the grain size [66]. In the current study, F_G was taken as the area fraction of grains with a size below 25 μm (from Fig. 5). The grain refinement kinetics in the hot-forged samples after different strain levels are represented in Fig. 11, which shows F_G as a function of total hot-forging strain. Regression analysis reveals that $K = 1.265 \pm 0.028$ and $n = 0.69 \pm 0.054$. This suggests that a hot forging strain, $\varepsilon > 4$ is sufficient to achieve almost complete recrystallization. However, this is unlikely to be accurate, since the rate of nucleation (number of nuclei per unit time per unit of volume) and rate of growth (length of growth per unit time) are not constant throughout hot forging process, but they are assumed to be constant when deriving Equation 3. In addition, the influence of the increasing grain size (d) will change the shape of the curve toward that the curve in Fig. 11 [66].

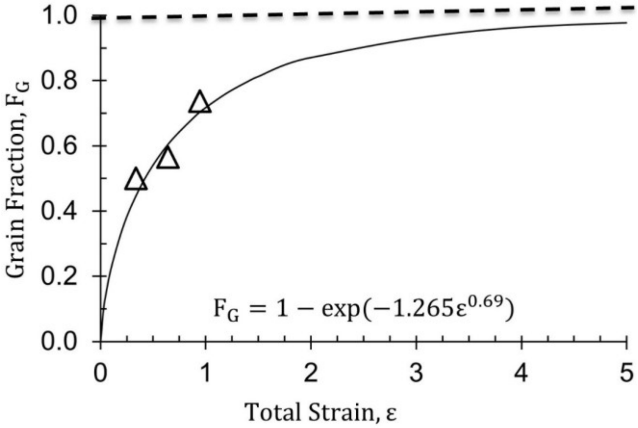

Fig. 11—The effect of strain magnitude on the fraction of refined grains (F_G) in the deformed samples

4.4. ***Effect of strain magnitude on the recrystallized grain size***

As the reduction of the sample cross section proceeds during deformation, it will lead to finer grain size, if the number of grains through the cross section of sample stays constant. Assuming that the transverse grain size follows the change in cross section of forged sample, the grain size can be represented by a simple function (indicated by dashed line in Fig. 12 and Equation 4, where d is the recrystallized grain size, d_0 in the solution-annealed grain size approximately $122\ \mu\mathrm{m}$, n is a materials-dependent constant and ε is the total forging strain). It is clearly seen in Fig. 12 that the transverse size of the grains decreases much faster than that of the whole sample in the range of relatively small strains below 0.45. The change in the grain size in largest strain follows a common tendency, which is characterized by a quasi-steady-state behavior, where the grain size becomes strain-invariant as reported for various metallic materials subjected to large strain deformation [68].

$$d = d_0 \exp(-n\varepsilon) \qquad \text{Equation 4}$$

In this study, regression analysis showed that $n = 2$. This value of n is remarkably higher than those of 1.2-1.4 in stainless steel with dynamically recrystallized microstructures [69,70]. For comparison, $n = 1$ in nickel [70].

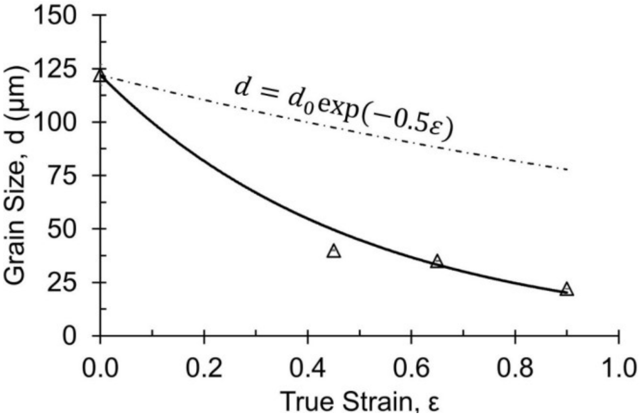

Fig. 12—Effect of the hot forging strain on the recrystallized austenite grain size (open triangles) and calculated (dashed line) values in Alloy 825 samples.

4.5. ***Evolution of dynamically recrystallized grains***

Grains with GOS $\leq 1.0°$ can be considered to be effectively free of dislocations [21] and are considered to be “recrystallized” [21] with no further deformation occurring within the grain after recrystallization. Following forging, there are significant populations of both recrystallized grains and non-recrystallized, deformed grains. Increasing the forging strain increases the fraction of grains that are classified as “deformed” but not recrystallized (Fig. 7), as well as increasing the fraction of grains that underwent recrystallization. It is probable that many of the grains that are identified as deformed did form by recrystallization but then underwent subsequent deformation. This deformation could cause the dislocation density to increase to the point that GOS $> 1.0°$. Other grains that do not undergo recrystallization will accumulate deformation during forging, so an increase in the frequency of “deformed” grains is not inconsistent with increased deformation and dynamic recrystallization. In a recent paper on the effect of strain on the evolution of microstructure during hot-forging of a nickel-based superalloy, the fraction of recrystallized grains was shown to increase with deformation [64]. In that case, the material was air-cooled at $1\,℃\,s^{-1}$ to room temperature. Static recovery and recrystallization would almost certainly occur during cooling. In the current study, all forged materials were quenched in water immediately after forging and so such mechanisms are suppressed. It would be expected that the continuous deformation keeps causing grains to recrystallize, after which they deform again, resulting in a large number of fine, “deformed” grains, as was observed (Fig. 7, Table 3). In the current material, the stacking fault energy, γ_{SFE} is calculated to 88 ± 5 mJ m^{-2} (Equation 2), which is significantly higher than those in which annealing twins have been found to block dislocations and so it is unlikely that the twins play a significant strengthening role. Therefore, twins may be ignored when evaluating strengthening mechanisms in the current alloy.

4.6. ***Hardness of deformed samples***

The hardness values averaged over 10 measurements on the solution-annealed sample was $1375 \pm 64\ \mathrm{MPa}$. Hardness is observed to increase with deformation strain (Fig. 13). Despite experimental scatter, represented by the error bars (one standard deviation about the mean value for each condition), the rise in hardness is significant.

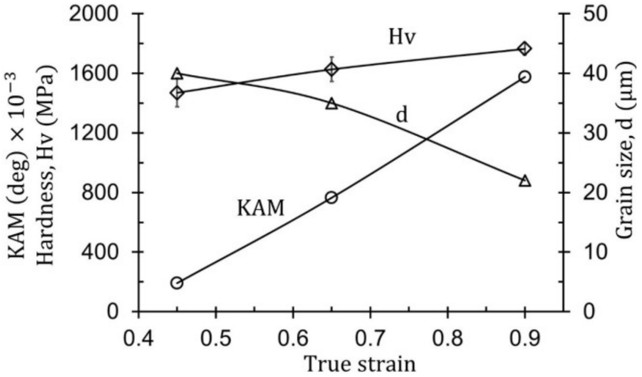

Fig. 13—Influence of strain magnitude on the average grain size, d, hardness, H_{V}, and the kernel average misorientation angle, θ_{KAM} in Alloy 825. Twin boundaries were excluded from the grain size calculation.

4.7. ***Strengthening mechanisms***

The relationship between the 0.2% proof strength ($\sigma_{0.2\%}$) and the recrystallized grain size is represented in Fig. 14. The current Alloy 825 samples processed by hot forging and subsequent water-quenching obey the following Hall-Petch-type relationship (Equation 5, where the 0.2% proof strength is expressed in MPa and the grain size, d, is measured in micrometres)

$$\sigma_{0.2} = (38 \pm 22) + (1.8 \pm 0.5) d^{-1/2} \qquad \text{Equation 5}$$

The data in Fig. 14 and Equation 5 suggest that there may be an additional strength contribution for the present samples, since the Hall-Petch coefficient (the grain size strengthening factor) has a large value of K_G = 1.8 MPa $m^{0.5}$, which is significantly large than those in other studies on Nickel-based superalloys (0.71–0.75 MPa $m^{0.5}$) [71–74] or austenitic stainless steels with statically recrystallized microstructures (0.27–0.64 MPa $m^{0.5}$) [75]. The correlation coefficient of linear regression for yield strength is 0.92, suggesting that the linear fit to the data is certainly reasonable.

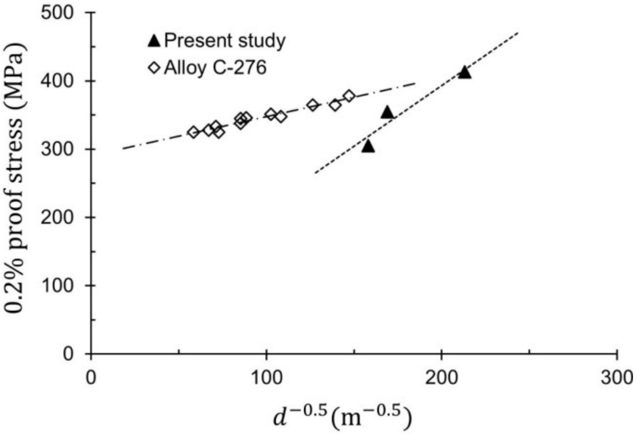

Fig. 14—The 0.2% proof stress ($\sigma_{0.2\%}$) of hot-forged as a function of the inverse of the square root of the average static grain size.

The additional strength contribution in the present study is very likely to be attributed to the high dislocation density (work hardening). This has been identified as the reason for the deviation from a Hall-Petch-type relationship of conventionally recrystallized austenitic stainless steels [75] or nickel-based superalloys [71–74] with relatively coarse grains. Assuming the strength contributions from grain boundaries and dislocations being independent and linearly additive, as has been reported elsewhere [76–80], the modified relationship for the offset yield strength should include an additional term for the dislocation strengthening, which is much similar to Taylor-type equation (Equation 6, where σ_0 is the inherent resistance of the material to dislocation glide excluding grain refinement and work hardening, α is a proportionality constant and depends on the strain rate and the temperature [81]; M is the Taylor factor, equal to 3.1 [82]; $G = 7.6 \times 10^{10}$ Pa is the shear modulus of the material [45], $b = 2.54 \times 10^{-10}$ m is the Burgers vector in the material, K_g is the Petch-coefficient and d is the grain size [83–88].

$$\sigma_\mathrm{y} = \sigma_0 + \alpha_\varepsilon MGb\rho^{1/2} + K_\mathrm{G}d^{-1/2} \qquad \text{Equation 6}$$

Using the relationship between KAM and dislocation density (Equation 1) and noting that those grains with low angle grain boundaries are likely to have a dislocation density that is orders of magnitude higher than other grains, a new expression for the yield strength can be derived to reformulate Equation 6 in terms of known or measureable quantities only (Equation 7). The second term of Equation 7 quantifies the contribution due to the low angle grain boundaries. Such boundaries form from dislocation substructures and so the effective size depends on dislocation density, which is related to the total strain. The dislocation density is measured from the kernel average misorientation data (Table 5). The final term gives the strengthening contribution from high angle grain boundaries.

$$\sigma_\mathrm{y} = \sigma_0 + \alpha_\varepsilon MGb((\kappa\theta_\mathrm{KAM}(bs)^{-1})_\mathrm{LAGB})^{1/2} + K_\mathrm{G}d_\mathrm{HAGB}{}^{-1/2} \qquad \text{Equation 7}$$

Table 5. Dislocation density, ρ, calculated using Table 1. Values of θ were measured during EBSD of the as-forged material and s is the step size of the EBSD scan.

Sample	$10^3\theta s^{-1}$ / m^{-1}	$10^{13}\rho$ / m^{-2}	$d^{-0.5}$ / m$^{0.5}$	$MGb\rho^{0.5}$ / MPa
A	1.11	0.875 ± 0.2	158.1	174.8
B	4.45	3.5 ± 0.3	169.0	349.5
C	9.16	7.2 ± 0.8	213.2	501.6

The relationship between the yield strength, grain size and dislocation density (Equation 6) can be used to derive the unknown parameters K_G, α_ε and σ_0. Combining the measured proof stresses, dislocation densities derived from KAM measurements and grain sizes from EBSD measurements (summarized in Table 4) and using Gaussian elimination gives the values of each quantity as: 0.42 MPa m$^{0.5}$, 0.26, and 193 MPa, respectively. The value of K_{G} is of the same magnitude of similar materials reported in literature [78,81,89–91] and so it is a reasonable result. The value of α_{ε} is slightly lower than published results for work-hardened austenitic stainless steels (~0.3) [76,91,92]. This is consistent with materials subjected to a stabilization treatment in which dislocations interact more weakly than work-hardened materials with internal stress fields caused by the accumulated dislocations [36]. The value of σ_0 is consistent with the strengthening mechanisms that contribute to it. The value of 193 MPa in the Hall-Petch equation is also reasonable. Almost the same values of around 200 MPa have frequently reported for austenitic steels by various authors [76,93,94].

An increase in the total strain leads to an increase in the grain boundary and dislocation strengthening, although the dislocation strengthening prevails over the grain size strengthening. Each contribution can be quantified ($\sigma_0 = 193\ \mathrm{MPa}$ from tensile test data, grain boundary strengthening and work hardening from Table 5 and Equation 7) and compared (Fig. 15).

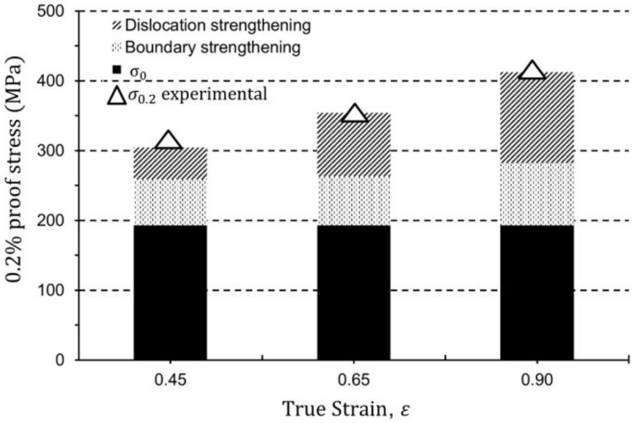

Fig. 15—Contribution of different strengthening mechanisms to general yield strength of hot forged Alloy 825 subjected to different strain levels.

Dislocation density will increase with the extent of deformation, as more dislocations are generated as strain proceeds up to some equilibrium level when recrystallization annihilates dislocations as quickly as they are produced. The dynamically recrystallized grain size decreases with an increase in deformation strain, as more grains contain sufficient dislocation density to drive the nucleation of new grains. It should, therefore, be possible to relate the dislocation density directly to recrystallized grain size. Indeed, analysis of the current data shows that the dislocation density, $\rho^{0.5}$, obeys a power law relationship with the dynamically recrystallized grain size, d_{DRX} (Equation 8).

$$\rho^{0.5} = 0.862\left(d_{\mathrm{DRX}}^{-0.5}\right)^{3.02} \qquad \text{Equation 8}$$

Substituting Equation 8 into Equation 7 and replacing the variables with the values derived in this section allows the calculation of 0.2% proof stress, $\sigma_{0.2,\mathrm{calc}}$, as a function of recrystallized grain size, d_{DRX} (Equation 9).

$$\sigma_{0.2,\mathrm{calc}} = 193 + 0.42 d_{\mathrm{DRX}}^{-0.5} + 1.3 \times 10^{-6} d_{\mathrm{DRX}}^{-1.5} \qquad \text{Equation 9}$$

Substituting Equation 4 into Equation 7 and replacing the variables with the values derived in this section and subsection 4.4 allows the prediction of 0.2% proof stress as a function of strain hardening, ε (Equation 10).

$$\sigma_{0.2} = 193 + [d_0 \exp(-n\varepsilon)]^{-0.5}\{0.42 + 1.3 \times 10^{-6}[d_0 \exp(-n\varepsilon)]^{-1}\} \qquad \text{Equation 10}$$

Where d_0 is initial grain size ($\sim 0.122\ \mathrm{m}$), $n = 2$ for Alloy 825, and ε is a true strain, equal to $\ln R_{\mathrm{R}}$ (reduction ratio). The experimental yield strengths are approximately one third higher than those calculated by Equation 10 (Fig. 16). Using regression, a constant factor of 1.34 leads to good agreement between the calculated and measured values, with a correlation coefficient, $R^2 = 0.99$.

$$\sigma_{0.2,\mathrm{exp}} = 1.34\sigma_{0.2,\mathrm{calc}} \qquad \text{Equation 11}$$

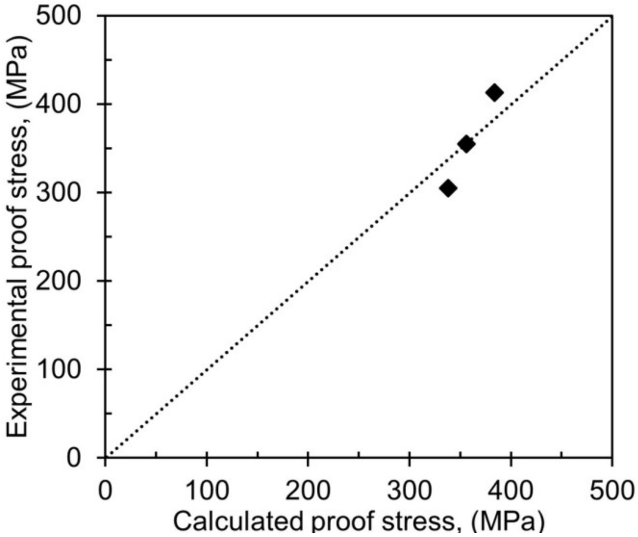

Fig. 16- Relationship between the experimental and calculated (Equation 11) proof strength of Alloy 825 samples subjected to different hot forging strain levels.

It is not apparent from the current data why the calculated proof stress is different to the measured value. Further tests are needed to improve the coefficients derived and to reduce statistical scatter. Both of these should improve the reliability of the derived model. However, it seems feasible to derive a relationship between the proof stress and reduction ratio during hot forging. This has the potential to allow customization of the process to achieve a desired proof stress.

4.8. ***Effect of strain magnitude on the dislocation density***

The dislocation density calculated by using KAM depends significantly on the OIM step size, the correct value of which depends, in turn, on the value of dislocation density [35]. For each sample, at least two EBSD scans with size step of 5 μm, 2.5 μm, 1.5 μm, 0.75 μm, 0.5 μm, 0.25 μm, and 0.1 μm was used to evaluate the θ_{KAM} value. For a constant dislocation density, the amount by which the KAM method underestimates the dislocation density increases as step size increases. Similarly, the underestimate increases at constant step size as the real dislocation density increases [35,95]. In this study, the KAM values increase as the hot-forged strain increases (Fig. 18), consistent with an increase in dislocation density as discussed previously (Fig. 17). The dislocation density can be considered as a unique source of internal stresses. It has been suggested that the measured dislocation densities (solid triangles in Fig. 17) during hot forging can be approximated by a maximum exponential growth function of true strain (solid lines in Fig. 17) (Equation 12, where ρ_0 is the dislocation density in solution annealed sample, ε is the true strain and β and n are materials constants) [80,96].

$$\rho = \rho_0 + \beta(1 - \exp(-n\varepsilon)) \qquad \text{Equation 12}$$

In the current study, $\rho_0 \approx 3.6 \times 10^{12}\ \mathrm{m}^{12}$. Regression reveals that the best estimate for $\beta = 8.8 \times 10^{13}\ \mathrm{m}^{-2}$ (cf. previously reported values of $20 \times 10^{15}\mathrm{m}^{-2}$ [80] and $5.75 \times 10^{15}\mathrm{m}^{-2}$ [96], both in austenitic stainless steels) and $n = 0.7$ (cf. previously reported values of 0.25 [80] and 1.03 [96]). The low value of β in the current alloy (Ni-based alloy) differs from the values reported for S304H austenitic stainless steel due to Alloy 825 has a stacking fault energy of approximately $88\ \mathrm{mJ\ m}^{-2}$ in contrast to the austenitic stainless steel, which has a low stacking fault energy of approximately 20 $\mathrm{mJ\ m}^{-2}$. Therefore, recovery should develop somewhat faster in nickel, compared to austenitic stainless steel, which then reduces dislocation density. In the steel, the deformation was performed at higher strain up to 4.0 and below 600 °C, but in the current study, there is a lower strain, which is induced at temperatures above 950 °C. This will allow dislocations to accumulate in the austenitic stainless steel, which can reduce the stacking fault energy in the different deformed samples [97,98].

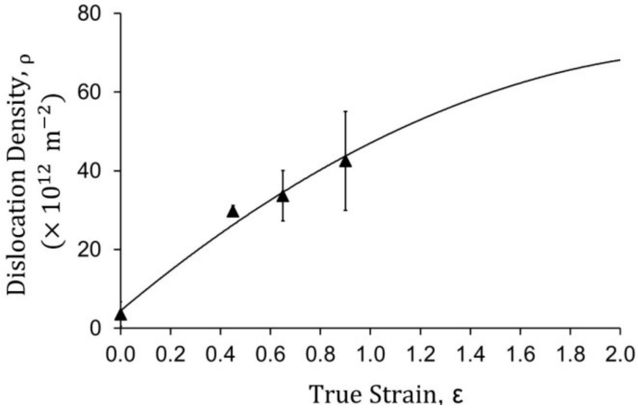

Fig. 17—The effect of forging strain level on the dislocation densities of experimental (solid triangle) and calculated (line, Equation 12) values in the present Alloy 825.

4.9. ***Chromium- and molybdenum-rich precipitates***

Fine precipitates could also be observed sparsely throughout the samples at grain boundaries after hot forging (Fig. 18a). These were analyzed using STEM-EDS and were found to be rich in chromium and molybdenum (Fig. 18b, Table 6). During analysis, these precipitates were found to be elongated along the boundaries with a length of between 150 nm and 500 nm. These findings are also consistent with other published studies in similar materials [9,99–101]. Furthermore, many annealing twins can also be seen in the hot-forged microstructure, which is also consistent with published studies of similar alloys [102,103]. While the presence of grain boundary precipitates could conceivably affect the subsequent behavior of the material, the volume fraction of precipitates is low and the grain boundary precipitates only occur sporadically in the material and so are unlikely to affect the bulk behavior and properties of the material to a significant extent.

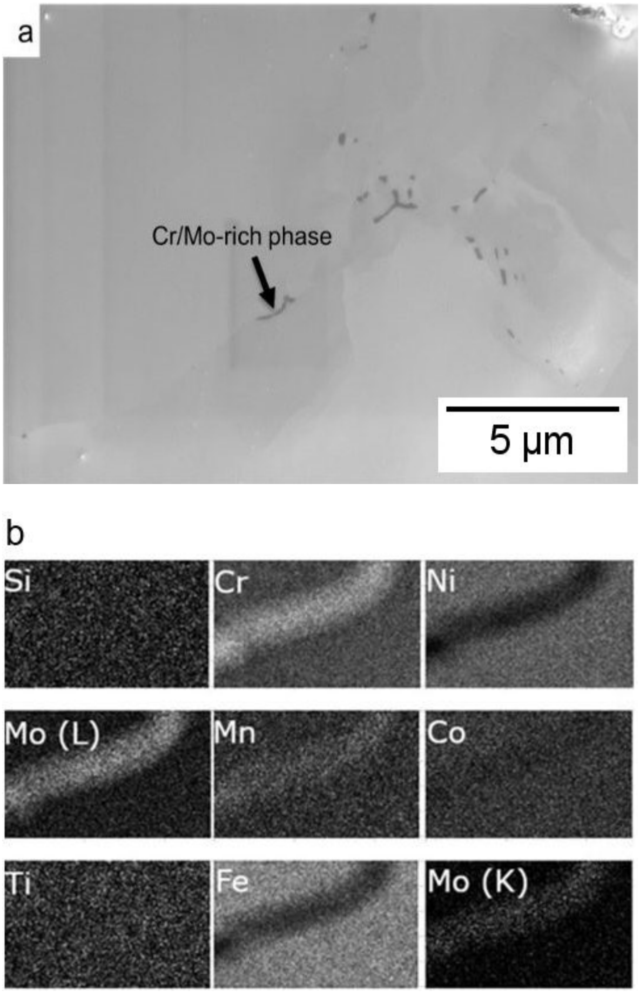
a
Cr/Mo-rich phase
5 µm
b
Si
Cr
Ni
Mo (L)
Mn
Co
Ti
Fe
Mo (K)

Fig. 18—SEM micrograph of initial billet before homogenization and forging: (a) precipitates decorating grain boundaries; (b) STEM-EDS mapping of elements in the precipitate indicated in (a).

Table 6: Chemical compositions (wt%) of the matrix and precipitate depicted in Fig. 19, measured using scanning TEM-EDS.

Element	Cr	Fe	Ni	Mo
GB phase	46.78	16.24	19.11	17.86
Matrix	23.98	32.73	40.13	3.16

5. **Conclusions**

The influence of strain magnitude on the mecrostructural evolution, texture and mechanical properties of Alloy 825 was studied. The main conclusions of this study are summarized below:

1) The average grain size decreases with increasing strain during forging, due to increased recrystallization. Both continuous and discontinuous dynamic recrystallization mechanisms operated during the hot forging process.
2) The area fraction of recrystallized grains ($\boldsymbol{F}_{\mathrm{G}}$) with sizes below 25 μm increased with increasing strain, ε. The fraction of grains that are recrystallized can be described using a simplified modification of the Johnson–Mehl–Avrami–Kolmogorov equation: $F_{\mathrm{G}} = 1 - \exp(-1.265\varepsilon^{0.69})$. This suggests that a near-fully recrystallized microstructure can be developed in the Alloy 825 tested at strains of ~ 4.
3) Hot forging results in nonrecrystallized grains oriented toward a $\langle 110 \rangle$ fiber forging texture, which is consistent with other face-centred cubic materials. An exception occurs at the highest strain level tested in this study (0.90), where the microstructure is only one-third recrystallized. In this deformation level, there is a $\langle 111 \rangle$ fibre texture.

4) The dislocation density of hot-forged samples increases with increased forging strain. In addition, the microstructures were characterized by high dislocation densities in deformed grains. The change in the dislocation density during hot forging may be expressed as

$$\rho = 5.39 \times 10^{12} + \beta(1 - \exp(-0.7\varepsilon)$$

where $\beta = 8.75 \times 10^{13}$ m^{-2} for deformed samples.

5) A power law function was obtained between the grain size, d and the dislocation density, ρ: $\rho^{0.5} = 0.862\left(d_{\mathrm{DRX}}^{-0.5}\right)^{3.02}$ for Alloy 825 processed by hot forging with different strain levels and subsequent water quenching. Both the grain size and substructural strengthening contributed to the mechanical properties. Thus, the yield strength could be expressed as a function of grain size by a modified Hall-Petch relationship:

$$\sigma_{0.2} = 193 + 0.42\mathrm{d}_{\mathrm{DRX}}^{-0.5} + 1.3 \times 10^{-6}\mathrm{d}_{\mathrm{DRX}}^{-1.5}.$$

6) The experimental 0.2% proof strength, $\sigma_{0.2}$, may be obtained by multiplying the calculated yield strength by a factor of 1.34 and can also be expressed through initial grain size, d_0, and total forging strain, ε, by modified Hall-Petch relationship:

$$\sigma_{0.2,\mathrm{calc}} = 193 + [d_0 \exp(-2\varepsilon)]^{-0.5}\{0.42 + 1.3 \times 10^{-6}[d_0 \exp(-2\varepsilon)]^{-1}\}$$

$$\sigma_{0.2,\mathrm{exp}} = 1.34\sigma_{0.2,\mathrm{calc}}$$

7) The maximum yield strength and ultimate tensile strength were obtained after forging to a true strain of 0.9 and were 413 MPa and 622 MPa, respecitvely, with a ductlity of 40%.

Acknowledgement

MA would like to thank Sandvik Materials Technology for the financial support, and the permission to publish this paper.

References

1 ASTM International: Standard Specification for Ni-Fe-Cr-Mo-Cu Alloy (UNS N08825 and UNS N08221)* Rod.

2 ASTM International: ASTM B564 - Nickel Alloy Forgings, www.astm.org.

3 ASTM International: Standard Specification for Nickel-Iron-Chromium-Molybdenum-Copper Alloy (UNS N08825 and N08221)* Seamless Pipe and Tube 1.

4 F.G. Hodge: *JOM*, 2006, vol. 58, pp. 28–31.

5 J. Botinha, J. Krämer, G. Genchev, C. Bosch, and H. Alves: in *Corrosion 2019*, 2019, pp. 1–12.

6 E.B.H. C.S. Tassen, G.D. Smith, S.K. Mannan: in *Corrosion 96*, 1996, pp. 1–10.

7 N. Alloys, H. Alloyed, S. Steels, F.O.R.H. Exchangers, O. Applications, and I.N. Chlorinated: in *Corrosion 2007*, vol. 59, 2007, pp. 1–20.

8 L. Shoemaker and J. Crum: in *Corrosion 2011*, 2011, pp. 1–13.

9 E. L. Raymond: in *Corrosion 68*, vol. 24, 1968, pp. 180–8.

10 M. Yu, J. Li, H. Tang, and Y. Bao: *J. Iron Steel Res. Int.*, 2011, vol. 18, pp. 68–72.

11 M. Al-Saadi, F. Sandberg, A. Kasarav, S. Jonsson, and P. Jönsson: *Procedia Manuf.*, 2018, vol. 15, pp. 1626–34.

12 M. Al-Saadi, F. Sandberg, C. Hulme-Smith, A. Karasev, and P.G. Jönsson: *J. Phys. Conf. Ser.*, 2019, vol. 1270, p. 012023.

13 L. Yang, Z. Geng, M. Zhang, and J. Dong: *Procedia Eng.*, 2012, vol. 27, pp. 997–1007.

14 Mitra Basirat: *Doctoral Thesis, KTH Royal Institute of Technology*, Stockholm, Sweden, 2013.

15 M. Nikura, K. Takahashi, and C. Ouchi: *Trans. Iron Steel Inst. Japan*, 1987, vol. 27, pp. 485–91.

16 R. Sandström and R. Lagneborg: *Scr. Metall.*, 1975, vol. 9, pp. 59–65.

17 C.M. Sellars and W.J. McG Tegart, C.M. Sellars, and W.J.M. Tegart: *Inter. Met. Rev.*, 1972, vol. 17, pp. 1–24.

18 J.J. Jonas, C.M. Sellars, and W.J.M. Tegart: *Metall. Rev.*, 1969, vol. 14, pp. 1–24.

19 T. Sakai, A. Belyakov, R. Kaibyshev, H. Miura, and J.J. Jonas: *Prog. Mater. Sci.*, 2014, vol. 60, pp. 130–207.

20 O. E. Hall: *Proc. Phys. Soc. Sect. B*, 1951, vol. 64, p. 742.

21 S. Raveendra, S. Mishra, K.V.M. Krishna, H. Weiland, and I. Samajdar: *Metall. Mater. Trans.*

A, 2008, vol. 39A, pp. 2760–71.

22 S. Mandal, P. V. Sivaprasad, and V.S. Sarma: *Mater. Manuf. Process.*, 2010, vol. 25, pp. 54–9.

23 D.P. Field, L.T. Bradford, M.M. Nowell, and T.M. Lillo: *Acta Mater.*, 2007, vol. 55, pp. 4233–41.

24 T. Konkova, S. Mironov, A. Korznikov, and S.L. Semiatin: *Mater. Sci. Eng. A*, 2011, vol. 528, pp. 7432–43.

25 S. Abolghasem, S. Basu, and M.R. Shankar: *J. Mater. Res.*, 2013, vol. 28, pp. 2056–69.

26 B. Aashranth, M. Arvinth Davinci, D. Samantaray, U. Borah, and S.K. Albert: *Mater. Des.*, 2017, vol. 116, pp. 495–503.

27 M.H. Alvi, S. Cheong, H. Weiland, and A.D. Rollett: *Mater. Sci. Forum*, 2004, vol. 467–470, pp. 357–62.

28 A. Hadadzadeh, F. Mokdad, M.A. Wells, and D.L. Chen: *Mater. Sci. Eng. A*, 2018, vol. 709, pp. 285–9.

29 ASTM E2627: *Astm Int.*, 2019, vol. 03.01, pp. 1–5.

30 A.P. Zhilyaev, I. Shakhova, A. Morozova, A. Belyakov, and R. Kaibyshev: *Mater. Sci. Eng. A*, 2016, vol. 654, pp. 131–42.

31 A.P. Zhilyaev, I. Shakhova, A. Belyakov, R. Kaibyshev, and T.G. Langdon: *Wear*, 2013, vol. 305, pp. 89–99.

32 Q. Liu, D. Juul Jensen, and N. Hansen: *Acta Mater.*, 1998, vol. 46, pp. 5819–38.

33 Y. Cao, H. Di, J. Zhang, J. Zhang, T. Ma, and R.D.K. Misra: *Mater. Sci. Eng. A*, 2013, vol. 585, pp. 71–85.

34 L.P. Kubin and A. Mortensen: *Scr. Mater.*, 2003, vol. 48, pp. 119–25.

35 M. Calcagnotto, D. Ponge, E. Demir, and D. Raabe: *Mater. Sci. Eng. A*, 2010, vol. 527, pp. 2738–46.

36 M. Odnobokova, Z. Yanushkevich, R. Kaibyshev, and A. Belyakov: *Materials (Basel).*, 2020, vol. 13, p. 2116.

37 D.. Brandon: *Acta Metall.*, 1966, vol. 14, pp. 1479–84.

38 J. Nordström, R. Siriki, J. Moverare, and G. Chai: *Mater. Sci. Forum*, 2018, vol. 941, pp. 1591–6.

39 ASM INTERNATIONAL: *ASM Metals Handbook*, 10th ed., 1990.

40 N. Harshavardhana, S.P.S.S. Sivam;, G. Kumar;, and A.K. Saxena; *Phys. Met. Metallogr.*, 2020, vol. Manscript, pp. 1–9.

41 S. Mitsche, P. Poelt, and C. Sommitsch: *J. Microsc.*, 2007, vol. 227, pp. 267–74.

42 V. Randle: *Acta Mater.*, 2004, vol. 52, pp. 4067–81.

43 J.K. Mackenzie: *Biometrika*, 1958, vol. 45, p. 229.

44 L. Alloys: Alloy 825 (Bar).

45 SpecialMetals: INCOLOY® alloy 825, http://www.specialmetals.com.

46 W.L. Mankins, S. Lamb, and I.A. International: in *Properties and Selection: Nonferrous Alloys and Special-Purpose Materials*, vol. 2, ASM International, 1990, pp. 428–45.

47 J.R. Davis, M.J. Donachie, R. Hartford, S.J. Donachie, and S.M. Corporation: *Met. Handb. Desk Ed.*, 2018, pp. 394–414.

48 I. Dempster, W.G. Forgings, and R. Wallis: *Heat Treat. Nonferrous Alloy.*, 2018, vol. 4, pp. 399–425.

49 I. Tamura, H. Sekine, T. Tanaka, and C. Ouchi: *Thermomechanical Process. High-Strength Low-Alloy Steels*, 2013, pp. 80–100.

50 T. Sakai and J.J. Jonas: *Acta Metall.*, 1984, vol. 32, pp. 189–209.

51 A. Belyakov, V. Torganchuk, O. V. Rybalchenko, S. V. Dobatkin, and R. Kaibyshev: *Mater. Sci. Forum*, 2021, vol. 1016, pp. 50–5.

52 J. Humphreys, G.S. Rohrer, and A. Rollett: *Recrystallization and Related Annealing Phenomena*, Second edi., Elsevier, Amsterdam, Netherlands, 2004.

53 O. Bouaziz and N. Guelton: *Mater. Sci. Eng. A*, 2001, vol. 319–321, pp. 246–9.

54 O. Bouaziz, S. Allain, and C. Scott: *Scr. Mater.*, 2008, vol. 58, pp. 484–7.

55 S. Kobayashi, S. Tsurekawa, T. Watanabe, and G. Palumbo: *Scr. Mater.*, 2010, vol. 62, pp.

294–7.

56 H. Yada, N. Matsuzu, K. Nakajima, K. Watanabe, and H. Tokita: *Trans. Iron Steel Inst. Japan*, 1983, vol. 23, pp. 100–9.

57 K. Huang and R.E. Logé: *Mater. Des.*, 2016, vol. 111, pp. 548–74.

58 X. ting Zhong, L. ke Huang, L. Wang, F. Liu, X. ming Dong, and Z. hua Zhang: *Trans. Nonferrous Met. Soc. China (English Ed.*, 2018, vol. 28, pp. 2294–306.

59 T. Sakai: *J. Mater. Process. Tech.*, 1995, vol. 53, pp. 349–61.

60 X.T. Zhong, L.K. Huang, and F. Liu: *J. Mater. Eng. Perform.*, 2020, vol. 29, pp. 6155–69.

61 S.P. Coryell, K.O. Findley, M.C. Mataya, and E. Brown: *Metall. Mater. Trans. A Phys. Metall. Mater. Sci.*, 2012, vol. 43, pp. 633–49.

62 M. Hasegawa, M. Yamamoto, and H. Fukutomi: *Acta Mater.*, 2003, vol. 51, pp. 3939–50.

63 C.B. Thomson and V. Randle: *Acta Mater.*, 1997, vol. 45, pp. 4909–16.

64 T. Konkova, S. Rahimi, S. Mironov, and T.N. Baker: *Mater. Charact.*, 2018, vol. 139, pp. 437–45.

65 X. Wang and W. Xiong: *Sci. Technol. Adv. Mater.*, DOI:10.1080/14686996.2020.1808433.

66 K. Barmak: *Metall. Mater. Trans. B Process Metall. Mater. Process. Sci.*, 2018, vol. 49, pp. 3616–80.

67 M. Odnobokova, A. Belyakov, N. Enikeev, R. Kaibyshev, and R.Z. Valiev: *Metals (Basel).*, 2020, vol. 10, p. 1614.

68 R. Pippan, S. Scheriau, A. Taylor, M. Hafok, A. Hohenwarter, and A. Bachmaier: *Annu. Rev. Mater. Res.*, 2010, vol. 40, pp. 319–43.

69 W. Roberts, H. Boden, and B. Ahlblom: *Met. Sci.*, 1979, vol. 13, pp. 195–205.

70 W. Roberts: *Microstructure Evolution and Flow Stress During Hot Working*, Pergamon Books Ltd.

71 Z. Jiang, J. Liu, and J. Lian: *Acta Metall. Mater.*, 1992, vol. 40, pp. 1587–97.

72 E.I. Galindo-Nava, L.D. Connor, and C.M.F. Rae: *Acta Mater.*, 2015, vol. 98, pp. 377–90.

73 R.W. Kozar, A. Suzuki, W.W. Milligan, J.J. Schirra, M.F. Savage, and T.M. Pollock: *Metall.*

Mater. Trans. A, 2009, vol. 40, pp. 1588–603.

74 J. Xu, H. Gruber, R. Boyd, S. Jiang, R.L. Peng, and J.J. Moverare: *Materialia*, 2020, vol. 10, p. 100657.

75 E. Pu, W. Zheng, Z. Song, K. Zhang, F. Yang, H. Lu, and H. Dong: *Mater. Sci. Eng. A*, 2017, vol. 705, pp. 335–47.

76 M. Odnobokova, A. Belyakov, and R. Kaibyshev: 2015, pp. 656–68.

77 D.A. Hughes and N. Hansen: *Acta Mater.*, 2000, vol. 48, pp. 2985–3004.

78 N. Hansen: *Scr. Mater.*, 2004, vol. 51, pp. 801–6.

79 R.Z. Valiev: *Mater. Trans.*, 2014, vol. 55, pp. 13–8.

80 I. Shakhova, A. Belyakov, Z. Yanushkevich, K. Tsuzaki, and R. Kaibyshev: *ISIJ Int.*, 2016, vol. 56, pp. 1289–96.

81 H. Mecking and U.F. Kocks: *Acta Metall.*, 1981, vol. 29, pp. 1865–75.

82 B. Verlinden, J. Driver, I. Samajdar, and R. Doherty: *Thermo-Mechanical Processing of Metallic Materials*, vol. Volume 11, Elsevier, 2007.

83 R. Armstrong, I. Codd, R.M. Douthwaite, and N.J. Petch: *Philos. Mag. A J. Theor. Exp. Appl. Phys.*, 1962, vol. 7, pp. 45–58.

84 E.O. Hall: *Proc. Phys. Soc. Sect. B*, 1951, vol. 64, pp. 747–53.

85 A. Cracknell and N.J. Petch: *Acta Metall.*, 1955, vol. 3, pp. 186–9.

86 M. Schneider, E.P. George, T.J. Manescau, T. Záležák, J. Hunfeld, A. Dlouhý, G. Eggeler, and G. Laplanche: *Int. J. Plast.*, 2020, vol. 124, pp. 155–69.

87 R.W. Armstrong: *Eng. Fract. Mech.*, 1987, vol. 28, pp. 529–38.

88 G.I. Taylor: *Proc. R. Soc. A Math. Phys. Eng. Sci.*, 1934, vol. 145, pp. 362–87.

89 Y. Matsuoka, T. Iwasaki, N. Nakada, and T. Tsuchiyama: 2013, vol. 53, pp. 1224–30.

90 S. Rajasekhara, P.J. Ferreira, L.P. Karjalainen, A. Kyro, and M. Society: DOI:10.1007/s11661-009-0072-2.

91 Z. Yanushkevich, A. Belyakov, R. Kaibyshev, C. Haase, and D.A. Molodov: *Mater. Charact.*, 2016, vol. 112, pp. 180–7.

92 Z. Yanushkevich, A. Mogucheva, M. Tikhonova, A. Belyakov, and R. Kaibyshev: *Mater. Charact.*, 2011, vol. 62, pp. 432–7.

93 Y.E. Shakhova, Z.C. Yanushkevich, and A.N. Belyakov: *Russ. Metall.*, 2012, vol. 2012, pp. 772–8.

94 C.M. Young and O.D. Sherby: *J Iron Steel Inst*, 1973, vol. 211, pp. 640–7.

95 M. Tikhonova, F. Brasche, A. Molodov, and A. Belyakov: DOI:10.1007/s11661-019-05340-8.

96 P. Kusakin, A. Belyakov, R. Kaibyshev, and D. Molodov: *IOP Conf. Ser. Mater. Sci. Eng.*, DOI:10.1088/1757-899X/63/1/012059.

97 K.K. Mehta, P. Mukhopadhyay, R.K. Mandal, and A.K. Singh: *Mater. Today Proc.*, 2015, vol. 2, pp. 1127–35.

98 D. Des, S. Solides, D.E. Nickel, E.T.D.E. Plomb, and I.N. Kupfer-: .

99 J.D. Busch, J.J. Debarbadillo, and M.J.M. Krane: 2013, vol. 44, pp. 5295–303.

100 Y.-M. Pan, D.S. Dunn, G.A. Cragnolino, and N. Sridhar: *Metall. Mater. Trans. A*, 2000, vol. 31, pp. 1163–73.

101 M.A. Shaikh, M. Iqbal, M. Ahmad, J.I. Akhtar, and K.A. Shoaib: *J. Mater. Sci. Lett.*, 1992, vol. 11, pp. 1009–11.

102 N. Bozzolo and M. Bernacki: *Metall. Mater. Trans. A Phys. Metall. Mater. Sci.*, 2020, vol. 51, pp. 2665–84.

103 B. Lin: 2015, p. 132.